



Editor's Choice



Using supervised machine learning methods to predict microfiber alignment and electrical conductivity of polymer matrix composite materials fabricated with ultrasound directed self-assembly and stereolithography

Karl Niendorf, Bart Raeymaekers*

Department of Mechanical Engineering, University of Utah, Salt Lake City, UT 84112, USA

ARTICLE INFO

Keywords:

Ultrasound directed self-assembly
Machine learning
polymer-matrix composites (PMCs)
Particle-reinforced composites
Electrical properties
3-D printing

ABSTRACT

Engineered polymer matrix composite materials with designer electrical properties are important for a myriad of engineering applications including flexible actuators and wearable sensors. We use stereolithography in combination with ultrasound directed self-assembly to align electrically conductive microfibers in a photopolymer matrix. We relate the fabrication process parameters to the resulting filler material alignment and corresponding electrical conductivity using supervised machine learning methods and quantify the prediction accuracy of data-driven models derived from different interpretable and non-interpretable algorithms. We determine that decision tree and artificial neural network algorithms result in data-driven models with R^2 scores that are 79.8% and 83.2% higher, respectively, than a traditional multivariate regression analysis benchmark model in predicting the microfiber alignment. Similarly, random forest and artificial neural network algorithms result in data-driven models that predict composite material electrical conductivity 9.1% and 13.7% more accurately, respectively, than a logistic multivariate regression benchmark model. Relating the fabrication process parameters to the resulting electrical conductivity of the material is a crucial step towards fabricating polymer matrix composite materials with designer electrical properties for use in engineering applications.

1. Introduction

Polymer matrix composite materials consist of a polymer matrix material and one or more continuous or discontinuous filler materials [1]. Continuous filler materials, such as carbon [2], glass [3], or Kevlar [4] fiber tow, orient in a user-specified direction under mechanical tension during fabrication and increase the mechanical properties of the composite material in the fiber direction [5]. Discontinuous filler materials, such as carbon nanotubes (CNTs) [6], spherical nanoscale particles [7], microscale platelets [8], or microfibers [9], either orient (angle) and organize (location) randomly [10] or align with each other in a user-specified orientation and organization [11] within the polymer matrix material. The orientation, organization, and material properties of the filler material, together with the properties of the matrix material, and the interaction between filler and matrix materials, determine the properties of the composite material [12].

To fabricate polymer matrix composite materials with filler material

in a user-specified orientation and organization, one must combine a technique to orient and organize the filler material with a method to form the macroscale matrix geometry of the material [13]. Conventional fabrication methods, such as mold casting [14] or injection molding [15], typically inject a mixture of resin and filler material into a hollow cavity or mold that constrains the material geometry. Alternatively, additive manufacturing (AM) methods, such as fused filament fabrication [16], direct ink writing [17], and stereolithography (SLA) [18], enable freeform polymer matrix composite material fabrication in a layer-by-layer fashion, without the use of a mold [19]. Furthermore, several methods exist to directly orient and organize discontinuous filler material in a polymer matrix material. For instance, shear force fields orient filler material in the shear direction [20] but require high-aspect-ratio filler material, and the method does not allow controlling the organization of the filler in the material. Alternatively, electric or magnetic fields allow controlling both the filler material orientation and organization but require electrically conductive or ferromagnetic filler

* Corresponding author.

E-mail address: bart.raeymaekers@utah.edu (B. Raeymaekers).

material and ultra-high external field strengths (on the order of 20 kV/m electric field [21] and 8000 mTesla magnetic field [22], respectively), which limits material choice and dimensional scalability. In contrast, ultrasound directed self-assembly (DSA) relies on the acoustic radiation force associated with a standing pressure (acoustic) wave to orient [23] and organize [24] filler material within a liquid matrix material. Ultrasound waves show low attenuation in low-viscosity fluids [25], and the acoustic radiation force is almost independent of the material properties and shape of the filler material [26].

Changing the orientation, organization, and material properties of the discontinuous filler material, in addition to the properties of the polymer matrix material, allows changing the physical properties of the polymer matrix composite material [27]. Correspondingly, one can engineer these materials to exhibit designer mechanical [28], thermal [29], or electrical [30] material properties, which is useful in the context of a myriad of engineering applications, such as stretchable strain sensors [31], combined sensors and actuators [32], chemical or biological sensors [33], and wearable electronics [34].

In this paper, we specifically focus on the electrical conductivity of polymer matrix composite materials. Orienting discontinuous filler material in a user-specified direction and aligning them with each other in the polymer matrix increases physical connectivity between individual filler material particles (e.g., electrically conductive microfibers), which decreases the percolation threshold [35] and increases the electrical conductivity in the alignment direction of the filler material [36]. Fabricating polymer matrix composite materials with designer electrical properties requires relating the electrical conductivity of the composite material to the filler material alignment and the corresponding fabrication process parameters. Several researchers have attempted to relate the composite material fabrication process parameters to the filler material alignment or the resulting electrical conductivity using interpolation of experimental results and regression analysis. For instance, using interpolation of experimental results, Ma et al. related the electrical conductivity to the weight percent w_f of CNTs ($0.5\% \leq w_f \leq 5\%$), aligned with a magnetic field in epoxy composite materials, and determined that the electrical conductivity increased with increasing w_f [37]. They also showed that electrical conductivity was highest in the CNT alignment direction and exceeded that of using randomly oriented CNTs. Similarly, Yunus et al. related the electrical conductivity of aligned and randomly oriented filler material to their weight percent ($0.5\% \leq w_f \leq 9.0\%$) in a photopolymer matrix material [7]. Chapkin et al. aligned CNTs in epoxy using an electric field and used regression analysis to show that the alignment of CNTs ($w_f = 0.005\%$) increased with increasing field strength (100 V/cm – 5000 V/cm) [38]. Niendorf and Raeymaekers combined stereolithography and ultrasound DSA to align carbon microfibers in photopolymer and used multivariate regression analysis to show that the alignment of carbon microfibers ($0.1\% \leq w_f \leq 0.5\%$) increased with increasing w_f and ultrasound field strength, and decreased with increasing distance between ultrasound transducers. In a later study, Niendorf and Raeymaekers used logistic multivariate regression analysis to characterize the electrical conductivity of photopolymer composite materials with ultrasonically aligned silver-coated glass microfibers ($1.0\% \leq w_f \leq 4.0\%$) and determined that increasing w_f and microfiber alignment increased the probability of the specimen conducting electricity [30].

The literature shows that first principles, interpolation of experimental results, and regression analysis can be used to derive models to predict filler material alignment and corresponding electrical conductivity of composite material specimens as a function of fabrication process parameters. However, these methods show critical limitations. Models derived using interpolation of experimental results assume a linear relationship between neighboring experimental data points. Furthermore, models derived using multivariate regression analysis consider parameter interaction effects that are limited to combinations of the most important effects [39], which can limit prediction accuracy in datasets with complex interactions or interactions that change within

the solution domain. In contrast, machine learning (ML) algorithms are well-suited to implement complex and changing physical relationships between dependent and independent parameters [40]. Therefore, the objective of this paper is to establish data-driven models that relate experimental data of microfiber alignment and electrical conductivity to the ultrasound DSA fabrication process parameters, using different interpretable and non-interpretable ML algorithms, and to evaluate their prediction accuracy compared to traditional multivariate regression models. These algorithms capture complex relationships between the fabrication process parameters (input) and corresponding microfiber alignment and electrical conductivity (output) of the composite material specimens and, thus, go beyond the knowledge that can be derived from multivariate regression analysis and interpolation of experimental results.

2. Materials and methods

2.1. Fabricating electrically conductive specimens with embedded lines of aligned microfibers

We use polymer matrix composite material specimens from our previous work, in which we employed multivariate regression analysis to characterize microfiber alignment and its corresponding electrical conductivity as a function of the ultrasound DSA fabrication process parameters [30].

Fig. 1 illustrates the ultrasound DSA and SLA process we use to fabricate composite material specimens with lines of aligned silver-coated glass microfibers (average diameter 15 μm , average length 130 μm , $\rho = 1,000 \text{ kg/m}^3$, Pottery Industries Inc. Conduct-O-Fil AG CLAD 12). First, an ultrasonic sonicator (Hielscher UP200Ht, 35.0 W, 5 min) disperses microfibers (weight percent $1.0 \leq w_f \leq 4.0\%$, measured before sonication) in photopolymer resin (viscosity = 250 cP, $c = 1305 \text{ m/s}$, Makerjuice Standard). Fig. 1 (a) shows a mixture of silver-coated glass microfibers dispersed in liquid photopolymer resin contained in an acrylic reservoir (30.4 mm \times 30.0 mm \times 6.0 mm) with two ultrasound transducers (PZT type SM111, center frequency $f_c = 1.5 \text{ MHz}$) separated by distance $d = 36\lambda$. Here $\lambda = c/f$ is the wavelength of the ultrasound wave and $f \approx f_c$ is the operating frequency. We energize the ultrasound transducers using a function generator (Tektronix AFG 3102) and radio frequency (RF) amplifier (E&I 2100L) to establish a standing ultrasound wave field in the reservoir. The acoustic radiation force associated with the standing ultrasound wave field organizes dispersed microfibers at the nodes of the standing wave, where they also orient along the nodes and align with each other [23]. Fig. 1(b) shows aligned silver-coated microfibers organized in parallel lines along the nodes of the standing ultrasound wave field. Finally, selective ultraviolet (UV) light curing solidifies the specimen geometry. Fig. 1 (c) depicts selective UV light exposure (data projector ViewSonic PJD7822HDL), which fixates the microfibers in their aligned and organized positions, and Fig. 1 (d) shows a typical composite material specimen (15.00 mm \times 10.00 mm \times 0.75 mm) with lines of aligned, electrically conductive silver-coated glass microfibers.

We use dimensional analysis and the Buckingham Pi theorem [41] to reduce the number of degrees of freedom of the ultrasound DSA process and minimize the number of experiments we must conduct. Specifically, three dimensionless fabrication process parameters describe the ultrasound DSA process: microfiber weight percent w_f , ultrasound transducer input power P , and ultrasound transducer separation distance D [42]. We use 138 composite material specimens fabricated using different treatment levels of w_f and P , with 10–20 specimen replications for each treatment level combination, to ensure statistically significant results [30]. Table 1 shows the ultrasound DSA fabrication process parameter treatment levels of the full factorial experiment used to fabricate the composite material specimens with different levels of microfiber alignment.

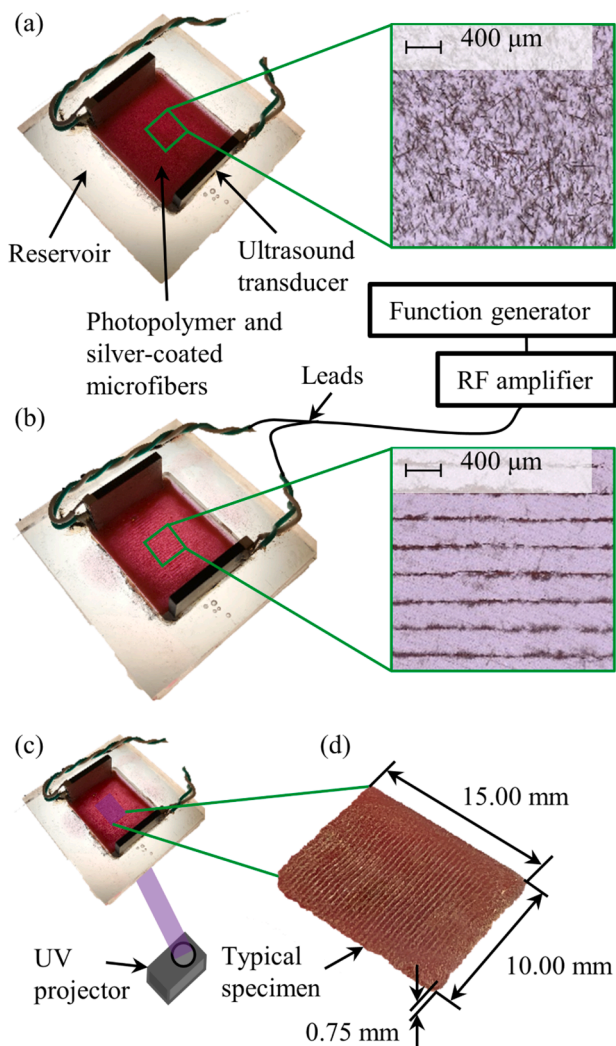


Fig. 1. Pictures of the ultrasound DSA and SLA fabrication process showing (a) silver-coated glass microfibers dispersed in photopolymer resin contained within an acrylic reservoir. (b) Microfibers align along the nodes of the standing ultrasound wave field, after energizing the ultrasound transducers with a function generator and RF amplifier. (c) Schematic illustration of selective UV curing of a composite material specimen and (d) a picture of a typical composite material specimen with lines of aligned microfibers.

Table 1

Dimensionless ultrasound DSA fabrication process parameter treatment levels used to fabricate 138 composite material specimens with aligned silver-coated glass microfibers [30].

Dimensionless fabrication process parameter	Treatment 1	Treatment 2	Treatment 3	Treatment 4
Microfiber weight percent, w_f	1.0	2.0	3.0	4.0
Ultrasound transducer input power, P	$2.87 \cdot 10^{13}$	$5.11 \cdot 10^{13}$	$1.07 \cdot 10^{14}$	N/A

2.2. Quantifying microfiber alignment and electrical conductivity

We sand and polish the top surface of each composite material specimen using sequentially finer abrasive polishing papers up to 1200 grit, to maintain a consistent surface finish of all specimens for optical

imaging and to expose the electrically conductive microfibers to measure electrical conductivity. We quantify microfiber alignment by calculating the microfiber alignment probability p_a according to the methodology documented in earlier work by our research group [42]. Briefly, we image (100x magnification, $2.47 \text{ mm} \times 2.47 \text{ mm}$ area) each specimen in the area that qualitatively shows the best microfiber alignment using an optical microscope (Keyence VHX-5000). We binarize the image and calculate the fast Fourier transform (FFT) anisotropy [43] to determine the alignment probability p_a , which represents the probability that microfibers organize at the nodes of the ultrasound standing wave field, i.e., parallel to the ultrasound transducers, orient along the nodes, and align with each other.

Fig. 2 illustrates the electrical resistance measurement (Mastech MY-65), from which we derive electrical conductivity by accounting for the total volume of silver in each material specimen, which depends on the microfiber weight percent w_f . It is well-known that contact resistance is an important consideration when quantifying the electrical resistivity or conductivity of polymer matrix composite materials with micro- or nanoscale filler material using a macroscale measurement device [44]. We minimize the contact resistance between the measurement probes and the composite material specimen by painting high-purity silver electrodes (SPI Supplies 05001-AB) along the edges of each specimen, such that each electrode covers approximately $2.5 \text{ mm} \times 15.0 \text{ mm}$, with the distance between both electrodes $L = 5.0 \text{ mm}$. Each electrode contacts all parallel lines of electrically conductive microfibers within the material specimen and, thus, we consider a single percolated microfiber network for each material specimen. We categorize a composite material specimen as electrically conductive if its conductivity exceeds $4.35 \cdot 10^{-4} \text{ S/m}$, which represents the minimum electrical conductivity of semi-conducting materials [45]. However, we note that the electrical conductivity of all electrically conductive specimens in this work varies between 31 and 793 S/m, i.e., the least conductive specimen is still five orders of magnitude more conductive than the cutoff value. Thus, slight variations in the magnitude of the electrical conductivity, resulting from contact resistance between the measurement probes and the silver electrodes, or between individual microfibers within a percolated microfiber network, do not influence the outcome of the measurement.

2.3. Dataset and supervised ML implementation

We use ML regression algorithms to derive data-driven models that predict microfiber alignment probability p_a as a function of w_f and P (dataset 1), and ML (binary) classification algorithms that create data-driven models to predict the probability that a composite material specimen is electrically conductive $p_{\text{conductive}}$ as a function of p_a and w_f (dataset 2). Both regression and classification ML algorithms are

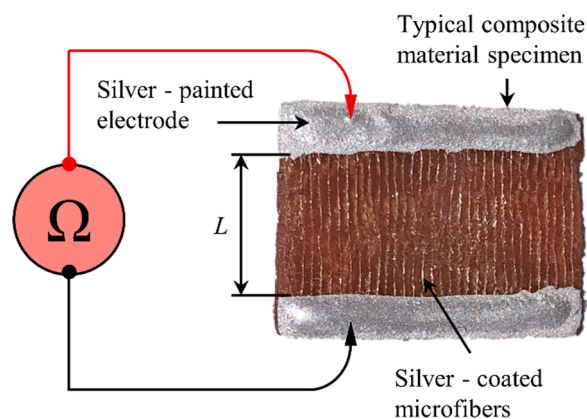


Fig. 2. Electrical resistance measurement of composite material specimens, showing a typical specimen with painted electrodes that contact all parallel lines of exposed silver-coated microfibers.

sensitive to the quality and integrity of the dataset, including missing, incorrect, or inconsistent data points [46]. We identify outliers according to the box plot rule, which categorizes data points according to their position within the quartiles of the dataset [47]. Therefore, we determine the lower (Q_1) and upper (Q_3) quartiles and the interquartile range ($IQR = Q_3 - Q_1$) of the alignment probability p_α for the composite material specimens fabricated with each treatment level (e.g., all specimens with $w_f = 2.0$). A data point is an outlier when it is $>1.5 \cdot IQR$ lower or higher than Q_1 or Q_3 , respectively, i.e., outside the middle 99.3% of observations [47]. We scale each independent parameter such that the maximum and minimum values are equal to one and zero, respectively, which allows the ML algorithms to treat parameters of different magnitudes equally. A hold-out method partitions each dataset into training and validation pools with a random 80/20 split, which reduces overfitting the model and ensures model validation with data not used to train the model [48].

We implement supervised ML algorithms using the open source scikit-learn toolbox in Python [49] and consider several interpretable ML algorithms that define explicit relationships or decisions between the ultrasound DSA fabrication process parameters (input parameters) and microfiber alignment or electrical conductivity (output parameter). These include linear and polynomial regression [50], Bayesian ridge regression [51], Gaussian Naïve Bayes [52], decision tree [53], random forest [54], and k -nearest neighbors (kNN) [55]. We use linear and polynomial regression to relate the fabrication process parameters to electrical conductivity according to the least-squares method. The Bayesian ridge regression algorithm works similar to linear regression but relies on probability distributions as data points rather than explicit point estimates. Gaussian Naïve Bayes creates a classifier model by estimating the probability that a specimen is electrically conductive according to the continuous, normally distributed, fabrication process parameters. Alternatively, the decision tree algorithm builds a model made up of nodes (parameter values), branches (decisions), and leaves (predictions). Subsequently, the random forest algorithm randomly divides the dataset to make multiple, smaller decision tree models and averages the predictions of all the trees. We optimize the data-driven models, created by the decision tree and random forest algorithms, to minimize prediction error by tuning the number of leaves per node, depth of tree, and pruning branches. In contrast, kNN creates a model that estimates microfiber alignment or electrical conductivity by calculating a weighted average of the k most similar points, and we tune a parameter weighting function and k to minimize the prediction error of the model.

We also implement non-interpretable ML algorithms that derive data-driven models without explicitly defining the relationship between input and output parameters, including support vector machine (SVM) and artificial neural network (ANN). SVM fits a multidimensional hyperplane through the data such that predictions minimize the error between alignment probability or electrical conductivity predictions and the experimental data. We optimize the SVM model to minimize its prediction error by changing the functions (kernel) to transform data such that it can be separated by the hyperplane. ANN creates a network of nonlinearly interconnected neurons consisting of an input layer, one or more hidden layers, and an output layer. We optimize the ANN model to minimize its prediction error by tuning the size of the hidden layer and by changing the solver that optimizes the parameter coefficients.

Common metrics to quantify the prediction error of data-driven models derived from regression and classification ML algorithms include the square of the correlation coefficient (R^2), root mean square error ($RMSE$), mean absolute error (MAE), accuracy score, precision, recall, and F_1 score [56]. A single metric may be sufficient to describe certain aspects of a model, but it is often desirable to consider multiple metrics to indicate model accuracy [57]. We calculate R^2 , $RMSE$, and MAE for each data-driven model resulting from the ML regression algorithms, where R^2 is given as

$$R^2 = 1 - \frac{\sum_{i=1}^n (a_i - p_i)^2}{\sum_{i=1}^n (a_i - \bar{a})^2} \quad (1)$$

such that a_i and p_i are the actual and predicted values of the i^{th} data point in the dataset of n data points and \bar{a} is the arithmetic mean of the actual dataset. Similarly, $RMSE$ is given as

$$RMSE = \sqrt{\frac{\sum_{i=1}^n (a_i - p_i)^2}{n}} \quad (2)$$

and MAE is given as

$$MAE = \frac{\sum_{i=1}^n |a_i - p_i|}{n} \quad (3)$$

Data-driven models derived from binary classification ML algorithms predict whether a composite material specimen is electrically conductive or insulating. The accuracy score is the ratio of the number of correct and total predictions, which is useful for a balanced dataset, i.e., with a similar number of electrically conductive and insulating specimens. The precision is the ratio of the number of correct predictions of electrically conductive specimens and the total number of predictions of conductive specimens. Recall is the ratio of the number of correct predictions of electrically conductive specimens and the total number of conductive specimens. The F_1 -score is the harmonic average of precision and recall.

$$F_1 - \text{score} = 2 \frac{\text{precision} \times \text{recall}}{\text{precision} + \text{recall}} \quad (4)$$

3. Results and discussion

3.1. Microfiber alignment probability

Table 2 shows the mean and standard deviation of the alignment probability p_α of all specimen replications fabricated with each w_f and P treatment level combination for dataset 1: $p_\alpha = f(w_f, P)$. We consider each data point, rather than the mean of specimen replications, for model training and evaluation.

Table 3 shows the evaluation metrics of the data-driven models derived from dataset 1 using interpretable and non-interpretable ML algorithms. We use multivariate regression analysis as a benchmark and compare models according to R^2 because it is a common metric, but also report the $RMSE$ and MAE .

From Table 3 we observe that all interpretable and non-interpretable ML algorithms, except linear and Bayesian ridge regression, result in higher R^2 and lower $RMSE$ and MAE values than those obtained with multivariate regression, indicating that the prediction error of the former models is smaller than that of the latter one. Linear and Bayesian ridge regression algorithms result in data-driven models with a higher prediction error than those derived from multivariate regression analysis, likely because these algorithms rely only on linear relationships between dependent and independent parameters, which may not capture the potentially complex relationships and interactions between the alignment probability p_α and the fabrication process parameters w_f and P . The polynomial ML regression algorithm uses regularization to tune

Table 2

Descriptive statistics of dataset 1 showing mean \pm standard deviation of the alignment probability p_α of all specimen replications fabricated with each w_f and P treatment level combination.

p_α	w_f [%]				
		1.0	2.0	3.0	4.0
P [-]	$2.87 \cdot 10^{13}$	0.42 ± 0.10	0.60 ± 0.11	0.40 ± 0.12	0.46 ± 0.14
	$5.11 \cdot 10^{13}$	0.48 ± 0.13	0.71 ± 0.09	0.58 ± 0.13	0.48 ± 0.05
—	$1.07 \cdot 10^{14}$	0.62 ± 0.06	0.68 ± 0.05	0.59 ± 0.09	0.50 ± 0.06

Table 3

Evaluation metrics of the data-driven models derived from dataset 1 using interpretable and non-interpretable ML algorithms.

Algorithm	R^2	RMSE	MAE
Multivariate regression (benchmark)	0.354	0.190	0.149
Interpretable ML algorithms			
Linear regression	0.261	0.218	0.172
Polynomial regression	0.559	0.169	0.139
Bayesian ridge regression	0.251	0.220	0.174
Decision tree	0.637	0.153	0.118
Random forest	0.562	0.168	0.137
k-nearest neighbors (kNN)	0.464	0.178	0.138
Non-interpretable ML algorithms			
Support vector machine (SVM)	0.608	0.159	0.134
Artificial neural network (ANN)	0.649	0.150	0.122

fourth order polynomial parameters, including interaction effects between w_f and P , such that the optimal model results in an R^2 value that is 57.8% higher than the multivariate regression benchmark. The decision tree algorithm yields a model with the highest R^2 of all models derived from interpretable ML algorithms, and the R^2 is 79.8% higher than that obtained with the multivariate regression benchmark. We use a decision tree with unrestricted tree depth such that each leaf predicts p_a for a minimum of one material specimen. Similarly, the random forest model averages the results of several decision trees [54], and we determine that the random forest that minimizes the prediction error consists of ten individual decision trees with unrestricted tree depth. The kNN algorithm derives a data-driven model that estimates alignment probability p_a by interpolating between the k most similar data points in the dataset. We determine that $k = 9$ minimizes the prediction error and results in an R^2 value that is 31.0% higher than the corresponding result obtained with the multivariate regression benchmark. This optimal k results from our specific dataset because we fabricate a minimum of $n = 10$ replications of each specimen for each combination of w_f and P . Thus, the algorithm interpolates between minimum $n - 1$ specimen replications.

The SVM algorithm derives a model with a prediction error similar to that of models derived with interpretable ML algorithms and we determine that the model that minimizes the prediction error relies on a radial basis function kernel [58]. ANN yields the most accurate model of both the non-interpretable and interpretable algorithms, with an R^2 that is 83.2% higher than the one obtained with the multivariate regression benchmark. We use an ANN with a hidden layer containing 50 neurons and optimize the model to minimize its prediction error using an LBFGS optimization solver [59].

Fig. 3 depicts the predicted microfiber alignment probability p_a (colorbar) as a function of ultrasound transducer input power P and

microfiber weight percent w_f , resulting from the decision tree model. Similarly, Fig. 4 depicts p_a (colorbar) as a function of P and w_f , resulting from the ANN model. The decision tree and ANN ML algorithms correspond to the interpretable and non-interpretable ML algorithms that result in models with the highest R^2 and smallest prediction error. The colored circular markers represent the average alignment probability p_a of all composite material specimen replications and (a) – (f) are optical images (scalebar = 200 μm) of typical composite material specimens of different w_f and P treatment level combinations, to relate the model prediction to the experimental data.

Figs. 3 and 4 show that p_a first increases and then decreases with increasing w_f and that p_a is maximum for $w_f = 2.0\%$. When $w_f < 2.0\%$, we observe that some microfibers may entangle but the acoustic radiation force still drives most microfibers to the nodes of the standing ultrasound wave field. Here, increasing w_f increases the number of microfibers that organize and align at the nodes of the standing ultrasound wave field, which increases p_a in the resulting composite material specimen. Figs. 3 and 4 (a) and (d) illustrate that the thickness of the lines of aligned microfibers increases when w_f increases from 1.0% to 2.0%, independent of P . These results quantitatively agree with those of Niendorf and Raeymaekers, who used multivariate regression analysis to show that p_a of carbon microfibers aligned in photopolymer resin increases with increasing w_f for $0.1\% \leq w_f \leq 0.5\%$ [42]. When $w_f \geq 2.0\%$, the nodes of the standing ultrasound wave field fill with microfibers such that individual microfibers entangle and interlock. Here, the acoustic radiation force does not overcome the mechanical interlocking and increasing $w_f > 2.0\%$ decreases p_a because some microfibers remain dispersed between the nodes of the standing ultrasound wave field. Figs. 3 and 4 (d) – (f) illustrate that individual microfibers interlock when w_f increases from 2.0% to 4.0%, which decreases p_a , independent of P . Scholz et al. reported similar results when using ultrasound DSA to align glass microfibers in epoxy [60]. They qualitatively observed that specimens with low w_f contained well-aligned microfibers whereas specimens with high w_f contained dense lines of interlocking and entangled microfibers. Figs. 3 and 4 also show that p_a increases with increasing P almost independent of w_f because increasing P increases the magnitude of the acoustic radiation force that drives microfibers towards the nodes of the standing ultrasound wave field, which increases p_a of the resulting composite material specimen. Figs. 3 and 4 (b) – (d) illustrate that increasing P from $5.11 \cdot 10^{13}$ to $1.07 \cdot 10^{14}$ reduces the thickness and increases the density of the lines of aligned microfibers, independent of w_f , which increases p_a . These results quantitatively agree with those documented by Chapkin et al., who used regression analysis to show that the alignment of CNTs in epoxy, using an electric field, increases with increasing electric field strength (100 – 5000 V/cm) [38].

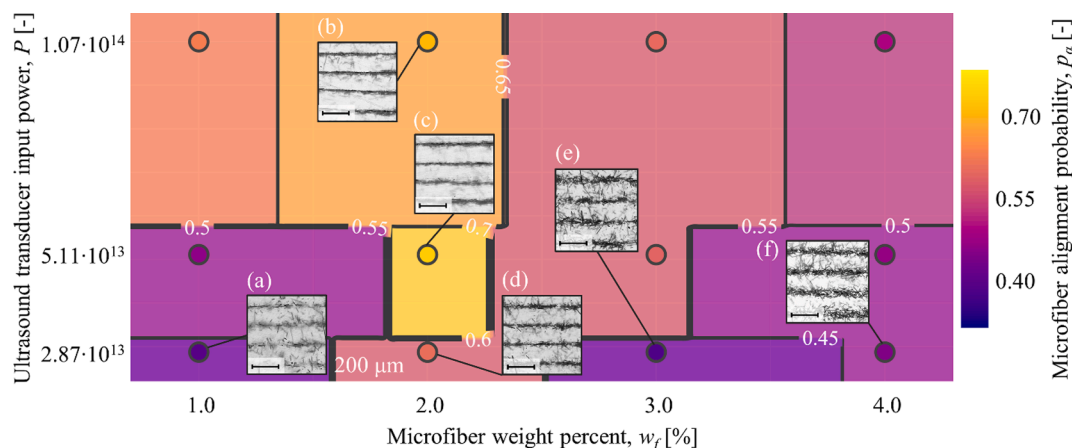


Fig. 3. Predicted microfiber alignment probability p_a (colorbar) as a function of ultrasound transducer input power P and microfiber weight percent w_f , resulting from the decision tree model. (a) – (f) display optical images (scalebar = 200 μm) of typical composite material specimens of different w_f and P treatment level combinations.

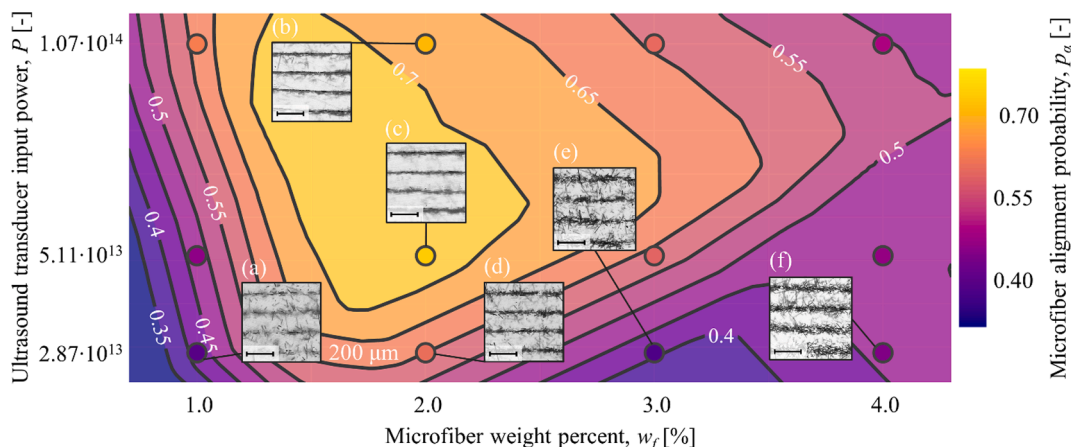


Fig. 4. Predicted microfiber alignment probability p_α (colorbar) as a function of ultrasound transducer input power P and microfiber weight percent w_f , resulting from the ANN model. (a) – (f) display optical images (scalebar = 200 μm) of typical composite material specimens of different w_f and P treatment level combinations.

Figs. 3 and 4 both show that P and w_f affect p_α , but the ANN model results in an R^2 score that is 1.9% higher than that of the decision tree model. The fundamental differences between decision tree (interpretable) and ANN (non-interpretable) algorithms derive data-driven models that predict different results for $p_\alpha = f(P, w_f)$. The contour lines that separate areas of discrete p_α values in Fig. 3 coincide with a constant value of P or w_f in a decision tree node, also known as a decision boundary, and the p_α prediction corresponds to a leaf at the end of a branch. The decision boundaries run parallel to the P or w_f axis because they remain constant for an entire branch and p_α predictions are constant in the area near individual data points because the model makes a discrete number of p_α predictions. Therefore, the number of constant p_α prediction regions is determined by the number of leaf nodes. In contrast, the ANN algorithm uses P and w_f to make continuous predictions of p_α . The models created by the decision tree and ANN algorithms both predict a maximum $p_\alpha = 0.70$, but the decision tree model predicts a minimum $p_\alpha = 0.45$ compared to 0.35 for the ANN model. However, qualitatively, the trend that p_α first increases and then decreases with increasing w_f and increases with increasing P are consistent for the models derived from both ML algorithms.

3.2. Electrical conductivity classification

Table 4 shows the evaluation metrics of the data-driven models derived from dataset 2 using interpretable and non-interpretable ML algorithms: $p_{\text{conductive}} = f(p_\alpha, w_f)$. We compare models according to accuracy score because it is a common metric and equally considers false positives and negatives [56], but we also report the model F_1 -score, $RMSE$, and MAE . We use a logistic multivariate regression analysis as a

Table 4

Evaluation metrics of the data-driven classification models derived using interpretable and non-interpretable ML algorithms, trained using dataset 2:

$$p_{\text{conductive}} = f(p_\alpha, w_f).$$

Model	Accuracy score	F_1 -score	RMSE	MAE
Logistic multivariate regression (benchmark)	0.786	0.700	0.463	0.214
Interpretable ML algorithms				
Logistic regression	0.821	0.828	0.423	0.179
Gaussian Naïve Bayes	0.750	0.800	0.500	0.250
Decision tree	0.821	0.848	0.423	0.179
Random forest	0.857	0.857	0.378	0.143
k -nearest neighbors (kNN)	0.786	0.824	0.463	0.214
Non-interpretable ML algorithms				
Support vector machine (SVM)	0.857	0.882	0.378	0.143
Artificial neural network (ANN)	0.893	0.909	0.327	0.107

performance benchmark, which yields an accuracy score of 0.714.

From Table 4 we observe that all interpretable and non-interpretable ML classification algorithms result in a higher accuracy score and F_1 -score and lower $RMSE$ and MAE value than those obtained using the logistic multivariate regression benchmark, indicating that the prediction error of the former models is smaller than that of the latter one. We optimize the ML logistic regression algorithm using L2 regularization, which creates a data-driven model with an accuracy score that is 4.5% higher than the logistic multivariate regression benchmark. The Gaussian Naïve Bayes algorithm derives a data-driven model with a lower accuracy score than the logistic multivariate regression benchmark, likely because it only relies on a linear relationship between the electrical conductivity $p_{\text{conductive}}$ and the ultrasound DSA fabrication process parameters p_α and w_f . The decision tree algorithm establishes a data-driven model with an accuracy score 4.5% higher than the logistic multivariate regression benchmark. A decision tree with unrestricted depth and a minimum of two samples per split minimizes the prediction error. The model derived from the random forest algorithm shows the highest accuracy score of the interpretable ML algorithms and is 9.1% higher than that of the logistic multivariate regression benchmark. The random forest that maximizes the accuracy score contains 50 individual trees with unrestricted depth and a minimum of two samples per split, like the optimal decision tree model. The k NN algorithm derives a data-driven model that predicts $p_{\text{conductive}}$ by comparing the k most similar data points in terms of p_α and w_f . When $k = 4$, the k NN algorithm results in a model with the same accuracy score as the logistic multivariate regression benchmark. This algorithm creates an accurate data-driven model when specimens fabricated with the same fabrication process parameter treatment levels are either all electrically conductive or insulating.

The SVM algorithm derives a model with an accuracy score similar to that of the model derived from the random forest algorithm, and we determine that the model that maximizes the accuracy score relies on a sigmoid kernel [61] and an L2 regularization penalty. The ANN algorithm yields the model with the highest accuracy score of all the non-interpretable and interpretable algorithms, which is 13.7% higher than the logistic multivariate regression benchmark. We use an ANN with a hidden layer containing 10 neurons and optimize the model to minimize its prediction error using an LBFGS optimization algorithm [59].

Fig. 5 shows the probability that a specimen is electrically conductive $p_{\text{conductive}}$ (colorbar) as a function of microfiber alignment probability p_α and microfiber weight percent w_f , resulting from the data-driven model derived from the random forest ML algorithm. Similarly, Fig. 6 depicts $p_{\text{conductive}}$ (colorbar) as a function of p_α and w_f , resulting from the data-driven model derived with the ANN ML algorithm. The

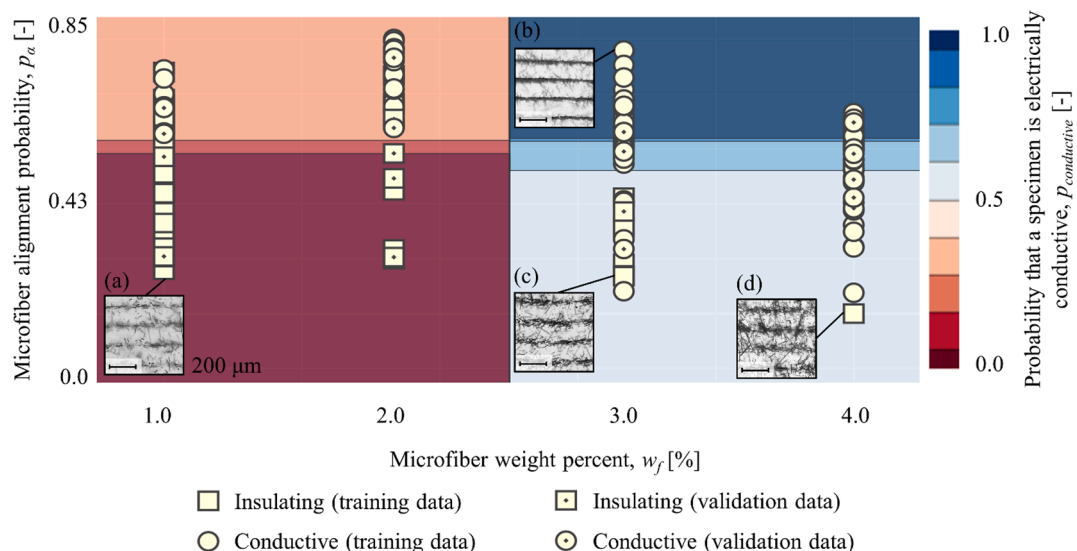


Fig. 5. Predicted probability that a composite material specimen is electrically conductive $p_{conductive}$ as a function of microfiber alignment probability p_{α} and microfiber weight percent w_f , resulting from the random forest model (interpretable ML algorithm with highest accuracy score). (a) – (d) display optical images (scalebar = 200 μm) of typical composite material specimens with different w_f and p_{α} combinations.

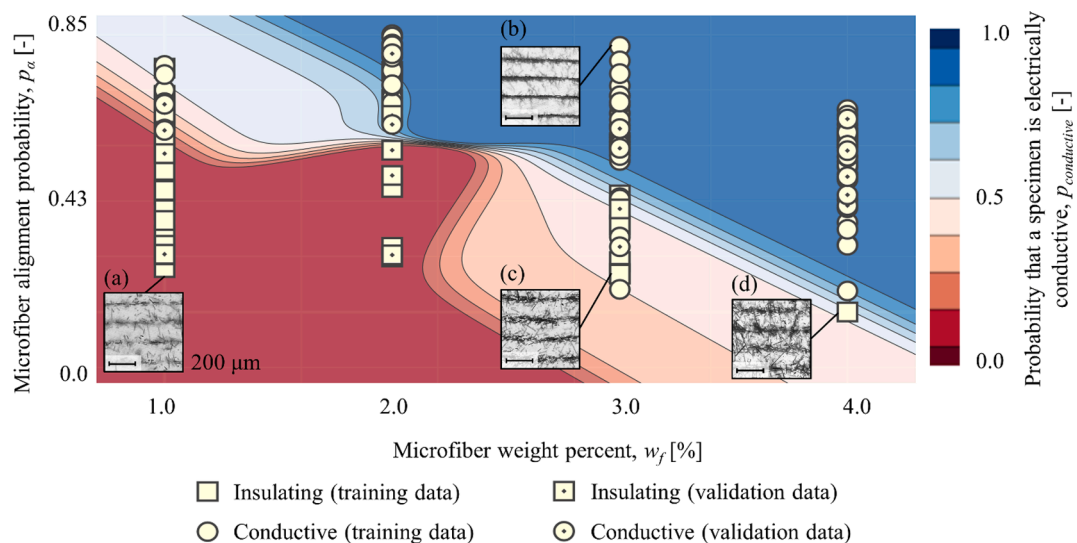


Fig. 6. Predicted probability that a composite material specimen is electrically conductive $p_{conductive}$ as a function of microfiber alignment probability p_{α} and microfiber weight percent w_f , resulting from the ANN model (non-interpretible ML algorithm with highest accuracy score). (a) – (d) display optical images (scalebar = 200 μm) of typical composite material specimens with different w_f and p_{α} combinations.

random forest and ANN data-driven models have the highest accuracy scores of models derived with interpretable and non-interpretible ML algorithms, respectively. The square and circular markers represent electrically insulating ($p_{conductive} = 0.0$) and conductive ($p_{conductive} = 1.0$) material specimens, respectively, solid markers indicate model training data, and dotted markers indicate validation data. Figs. 5 and 6(a) – (d) show typical composite material specimens (scalebar = 200 μm) with different p_{α} and w_f , illustrating the effect of the ultrasound DSA fabrication process parameters on the arrangement of and interaction between individual microfibers.

A composite material specimen is electrically conductive when a long-range percolated network of interconnected conductive microfibers exists. Figs. 5 and 6 show that the probability that a specimen forms a percolated microfiber network $p_{conductive}$ increases with increasing p_{α} and w_f . The density of microfibers organized and aligned at the nodes of the standing ultrasound wave field increases with increases p_{α} , which increases the probability that individual microfibers make

contact and establish a long-range percolated network, independent of w_f . Figs. 5 and 6 (b) and (c) illustrate that when p_{α} increases from 0.22 (Figs. 5 and 6(c)) to 0.77 (Figs. 5 and 6 (b)) with $w_f = 3.0\%$, $p_{conductive}$ increases from 0.6 to 1.0 (random forest model – Fig. 5) and from 0.5 to 0.9 (ANN model – Fig. 6). Thus, increasing p_{α} with constant w_f reduces the percolation threshold by increasing the microfiber density at the nodes of the standing ultrasound wave field and, therefore, contact between microfibers. Similarly, increasing w_f increases the number of microfibers within a composite material specimen, which increases the probability that microfibers contact and form an electrically conductive network, independent of p_{α} . Figs. 5 and 6 (a) and (d) illustrate specimens with poorly aligned microfibers, i.e., $p_{\alpha} = 0.26$ and 0.17, respectively. When increasing w_f from 1.0% (Figs. 5 and 6 (a)) to 4.0% (Figs. 5 and 6 (d)), $p_{conductive}$ increases from 0.0 to 0.6 (random forest model – Fig. 5) and from 0.1 to 0.55 (ANN model – Fig. 6). These results agree with Ma et al. who reported that electrical conductivity increases with increasing CNT w_f ($0.5\% \leq w_f \leq 5\%$) in epoxy composite materials with

magnetically aligned CNTs [37]. They also reported that electrical conductivity approaches an asymptote when $w_f > 3.0\%$, which is similar to the predictions of our random forest model, which indicates that $p_{conductive}$ is constant when $w_f > 2.5\%$ for a specific p_α . Similarly, Yunus et al. found that electrical conductivity increases with increasing w_f in photopolymer composite materials with ultrasonically aligned or randomly oriented filler material ($0.5\% \leq w_f \leq 9.0\%$) [7]. This suggests that increasing either p_α or w_f increases the probability of forming a percolated microfiber network, which is consistent with our results.

We observe from Fig. 5 that the random forest model predicts four distinct regions of $p_{conductive}$, with a small gradient along the p_α axis. These regions of constant $p_{conductive}$ correspond to the averages of discrete predictions of individual decision trees in the random forest. The boundaries separating those regions are parallel to the p_α or w_f axis because the individual decision trees that make up the random forest assign predictions based on constant parameter value boundaries (e.g., $w_f = 2.5\%$). We observe from Fig. 6 that the ANN model predicts $p_{conductive}$ to follow smooth nonlinear curves that result in an accuracy score 4.2% higher than the random forest model. This is because the ANN model makes continuous predictions that consider non-linear relationships between all training data rather than splitting data according to proximity.

4. Conclusions

We implement interpretable and non-interpretable machine learning algorithms to derive data-driven models that characterize microfiber alignment probability p_α as a function of the ultrasound DSA fabrication process parameters w_f and P . The most accurate models derive from decision tree and artificial neural network algorithms, which result in R^2 scores that are 79.8% and 83.2% higher than the multivariate regression analysis benchmark, respectively. p_α increases with increasing ultrasound transducer input power P because increasing P increases the strength of the acoustic radiation force that drives microfibers to the nodes of the standing ultrasound wave field, which is consistent with our previous findings obtained using multivariate regression analysis [42]. We also find that p_α increases and then decreases with increasing microfiber weight percent w_f . When $w_f < 2.0\%$, increasing w_f increases the number of microfibers at the nodes of the standing ultrasound wave field, which renders the lines of aligned microfibers thicker and darker. When $w_f \geq 2.0\%$, the nodes of the standing ultrasound wave field fill with microfibers, causing individual microfibers to interlock, which prevents additional microfibers from aligning.

Data-driven models derived from random forest and ANN algorithms are 9.1% and 13.7% more accurate, respectively, at predicting the probability that a composite material specimen is electrically conductive $p_{conductive}$, as a function of p_α and w_f , compared to the logistic multivariate regression benchmark. $p_{conductive}$ increases with increasing p_α and w_f , which is consistent with results from our previous work [30]. Increasing either p_α or w_f increases the number of microfibers at the nodes of the standing ultrasound wave field, which increases the interaction between individual microfibers and, therefore, the probability of establishing a long-range percolated microfiber network. We also determine that increasing p_α reduces the percolation threshold by increasing the local w_f , and therefore the interaction between microfibers, at the nodes of the standing ultrasound wave field.

Using data-driven models derived from machine learning algorithms to predict microfiber alignment and electrical conductivity classification as a function of ultrasound DSA fabrication process parameters is an important step towards using ultrasound DSA to manufacture engineered composite materials with embedded electrical wiring and anisotropic electrical properties, for use in applications such as wearable robotics or stretchable strain sensors.

CRedit authorship contribution statement

Karl Niendorf: Methodology, Validation, Formal analysis, Investigation, Visualization, Writing – original draft. **Bart Raeymaekers:** Conceptualization, Methodology, Formal analysis, Visualization, Writing – review & editing, Supervision, Project administration, Funding acquisition.

Declaration of Competing Interest

The authors declare that they have no known competing financial interests or personal relationships that could have appeared to influence the work reported in this paper.

Acknowledgments

This research was supported by the National Science Foundation under award no. 2017588.

References

- [1] S.-J. Park, M.-K. Seo, Chapter 7 - Types of Composites, in: Interface Sci. Technol., 2011: pp. 501–629.
- [2] Q. He, H. Wang, K. Fu, L. Ye, 3D printed continuous CF/PA6 composites: Effect of microscopic voids on mechanical performance, Compos. Sci. Technol. 191 (2020), 108077, <https://doi.org/10.1016/j.compscitech.2020.108077>.
- [3] Y. Ming, Z. Xin, J. Zhang, Y. Duan, B. Wang, Fabrication of continuous glass fiber-reinforced dual-cure epoxy composites via UV-assisted fused deposition modeling, Compos. Commun. 21 (2020), 100401, <https://doi.org/10.1016/j.coco.2020.100401>.
- [4] G.W. Melenka, B.K.O. Cheung, J.S. Schofield, M.R. Dawson, J.P. Carey, Evaluation and prediction of the tensile properties of continuous fiber-reinforced 3D printed structures, Compos. Struct. 153 (2016) 866–875, <https://doi.org/10.1016/j.compstruct.2016.07.018>.
- [5] S.M.F. Kabir, K. Mathur, A.F.M. Seyam, A critical review on 3D printed continuous fiber-reinforced composites: History, mechanism, materials and properties, Compos. Struct. 232 (2020), 111476, <https://doi.org/10.1016/j.compstruct.2019.111476>.
- [6] N.P. Singh, V.K. Gupta, A.P. Singh, Graphene and carbon nanotube reinforced epoxy nanocomposites: A review, Polymer (Guildf). 180 (2019) 121724, <https://doi.org/10.1016/j.polymer.2019.121724>.
- [7] D.E. Yunus, S. Sohrabi, R. He, W. Shi, Y. Liu, Acoustic patterning for 3D embedded electrically conductive wire in stereolithography, J. Micromech. Microeng. 27 (2017), <https://doi.org/10.1088/1361-6439/aa62b7>.
- [8] R. Libanori, R.M. Erb, A.R. Studart, Mechanics of platelet-reinforced composites assembled using mechanical and magnetic stimuli, ACS Appl. Mater. Interfaces. 5 (21) (2013) 10794–10805, <https://doi.org/10.1021/am402975a>.
- [9] T. Sugama, K. Gawlik, Milled carbon microfiber-reinforced poly(phenylenesulfide) coatings for abating corrosion of carbon steel, Polym. Polym. Compos. 11 (2003) 161–169, <https://doi.org/10.1177/096739110301100301>.
- [10] B. Herren, P. Larson, M. Saha, Y. Liu, Enhanced Electrical Conductivity of Carbon Nanotube-Based Elastomer Nanocomposites Prepared by Microwave Curing, Polymers (Basel). 11 (2019) 1212, <https://doi.org/10.3390/polym11071212>.
- [11] P.S. Goh, A.F. Ismail, B.C. Ng, Directional alignment of carbon nanotubes in polymer matrices: Contemporary approaches and future advances, Compos. Part A Appl. Sci. Manuf. 56 (2014) 103–126, <https://doi.org/10.1016/j.compositesa.2013.10.001>.
- [12] W. Xu, S. Jambhulkar, D. Ravichandran, Y. Zhu, M. Kakarla, Q. Nian, B. Azeredo, X. Chen, K. Jin, B. Vernon, D.G. Lott, J.L. Cornella, O. Shefi, G. Miquelard-Garnier, Y. Yang, K. Song, 3D Printing-Enabled Nanoparticle Alignment: A Review of Mechanisms and Applications, Small 2100817 (2021) 2100817, <https://doi.org/10.1002/sml.202100817>.
- [13] K. Niendorf, B. Raeymaekers, Additive Manufacturing of Polymer Matrix Composite Materials with Aligned or Organized Filler Material : A Review, Adv. Eng. Mater. 2001002 (2021) 1–18, <https://doi.org/10.1002/adem.202001002>.
- [14] J. Delmonte, Molding and Casting of Metal/Polymer Composites, in: Met. Compos., Springer US, Boston, MA, 1990. 10.1007/978-1-4684-1446-2_3.
- [15] S.-Y. Fu, B. Lauke, E. Mäder, C.-Y. Yue, X. Hu, Tensile properties of short-glass-fiber- and short-carbon-fiber-reinforced polypropylene composites, Compos. Part A Appl. Sci. Manuf. 31 (10) (2000) 1117–1125, [https://doi.org/10.1016/S1359-835X\(00\)00068-3](https://doi.org/10.1016/S1359-835X(00)00068-3).
- [16] B. Brenken, E. Barocio, A. Favaloro, V. Kunc, R.B. Pipes, Fused filament fabrication of fiber-reinforced polymers: A review, Addit. Manuf. 21 (2018) 1–16, <https://doi.org/10.1016/j.addma.2018.01.002>.
- [17] M. Wei, F. Zhang, W. Wang, P. Alexandridis, C. Zhou, G. Wu, 3D direct writing fabrication of electrodes for electrochemical storage devices, J. Power Sour. 354 (2017) 134–147, <https://doi.org/10.1016/j.jpowsour.2017.04.042>.
- [18] J.Z. Manapat, Q. Chen, P. Ye, R.C. Advincula, 3D Printing of Polymer Nanocomposites via Stereolithography, Macromol. Mater. Eng. 302 (9) (2017) 1600553, <https://doi.org/10.1002/mame.v302.910.1002/mame.201600553>.

- [19] I. Gibson, D. Rosen, B. Stucker, *Additive Manufacturing Technologies: 3D Printing, Rapid Prototyping, and Direct Digital Manufacturing*, 2nd ed., Springer, US, 2015.
- [20] G. Postiglione, G. Natale, G. Griffini, M. Levi, S. Turri, Conductive 3D microstructures by direct 3D printing of polymer/carbon nanotube nanocomposites via liquid deposition modeling, *Compos. Part A Appl. Sci. Manuf.* 76 (2015) 110–114, <https://doi.org/10.1016/j.compositesa.2015.05.014>.
- [21] P.V. Kamat, K.G. Thomas, S. Barazzouk, G. Girishkumar, K. Vinodgopal, D. Meisel, Self-assembled linear bundles of single wall carbon nanotubes and their alignment and deposition as a film in a dc field, *J. Am. Chem. Soc.* 126 (34) (2004) 10757–10762, <https://doi.org/10.1021/ja0479888>.
- [22] Y. Tanimoto, M. Fujiwara, Y. Shimomura, I. Mukouda, E. Oki, M. Hamada, Magnetic Orientation and Magnetic Properties of a Single Carbon Nanotube, *J. Phys. Chem. A* 105 (2002) 4383–4386, <https://doi.org/10.1021/jp004620y>.
- [23] M. Prisbrey, B. Raeymaekers, Aligning High-Aspect-Ratio Particles in User-Specified Orientations with Ultrasound-Directed Self-Assembly, *Phys. Rev. Appl.* 12 (2019), 014014, <https://doi.org/10.1103/PhysRevApplied.12.014014>.
- [24] M. Prisbrey, J. Greenhall, F. Guevara Vasquez, B. Raeymaekers, Ultrasound directed self-assembly of three-dimensional user-specified patterns of particles in a fluid medium, *J. Appl. Phys.* 121 (2017), <https://doi.org/10.1063/1.4973190>.
- [25] L.E. Kinsler, A.R. Frey, A.B. Coppens, J.V. Sanders, *Fundamentals of Acoustics*, John Wiley, New York, 2000.
- [26] R.R. Collino, T.R. Ray, R.C. Fleming, C.H. Sasaki, H. Haj-Hariri, M.R. Begley, Acoustic field controlled patterning and assembly of anisotropic particles, *Extrem. Mech. Lett.* 5 (2015) 37–46, <https://doi.org/10.1016/j.eml.2015.09.003>.
- [27] S. Shabaniverki, J.J. Juárez, Directed Assembly of Particles for Additive Manufacturing of Particle-Polymer Composites, *Micromachines*. 12 (8) (2021) 935, <https://doi.org/10.3390/mi12080935>.
- [28] J. Greenhall, L.J. Homel, B. Raeymaekers, Ultrasound directed self-assembly processing of nanocomposites with ultra-high carbon nanotube weight fractions, *J. Compos. Mater.* 53 (2018), <https://doi.org/10.1177/0021998318801452>.
- [29] L. Lu, Z. Zhang, J. Xu, Y. Pan, 3D-printed polymer composites with acoustically assembled multidimensional filler networks for accelerated heat dissipation, *Compos. Part B Eng.* 174 (2019), <https://doi.org/10.1016/j.compositesb.2019.106991>.
- [30] K. Niendorf, B. Raeymaekers, Combining ultrasound directed self-assembly and stereolithography to fabricate engineered polymer matrix composite materials with anisotropic electrical conductivity, *Compos. Part B*. 223 (2021), 104743, <https://doi.org/10.1016/j.compositesb.2021.109096>.
- [31] I. Kang, M.J. Schulz, J.H. Kim, V. Shanov, D. Shi, A carbon nanotube strain sensor for structural health monitoring, *Smart Mater. Struct.* 15 (3) (2006) 737–748, <https://doi.org/10.1088/0964-1726/15/3/009>.
- [32] S. Sharafkhani, M. Kokabi, Ultrathin-shell PVDF/CNT nanocomposite aligned hollow fibers as a sensor/actuator single element, *Compos. Sci. Technol.* 200 (2020), 108425, <https://doi.org/10.1016/j.compscitech.2020.108425>.
- [33] W. Cheung, P.L. Chiu, R.R. Parajuli, Y. Ma, S.R. Ali, H. He, Fabrication of high performance conducting polymer nanocomposites for biosensors and flexible electronics: Summary of the multiple roles of DNA dispersed and functionalized single walled carbon nanotubes, *J. Mater. Chem.* 19 (2009) 6465–6480, <https://doi.org/10.1039/b823065j>.
- [34] S. Park, M. Vosguerichian, Z. Bao, A review of fabrication and applications of carbon nanotube film-based flexible electronics, *Nanoscale*. 5 (2013) 1727–1752, <https://doi.org/10.1039/c3nr33560g>.
- [35] R.B. Ladani, S. Wu, A.J. Kinloch, K. Ghorbani, J. Zhang, A.P. Mouritz, C.H. Wang, Multifunctional properties of epoxy nanocomposites reinforced by aligned nanoscale carbon, *Mater. Des.* 94 (2016) 554–564, <https://doi.org/10.1016/j.matdes.2016.01.052>.
- [36] A. Chanda, S.K. Sinha, N.V. Datla, Electrical conductivity of random and aligned nanocomposites: Theoretical models and experimental validation, *Compos. Part A*. 149 (2021), 106543, <https://doi.org/10.1016/j.compositesa.2021.106543>.
- [37] C. Ma, H.Y. Liu, X. Du, L. Mach, F. Xu, Y.W. Mai, Fracture resistance, thermal and electrical properties of epoxy composites containing aligned carbon nanotubes by low magnetic field, *Compos. Sci. Technol.* 114 (2015) 126–135, <https://doi.org/10.1016/j.compscitech.2015.04.007>.
- [38] W.A. Chapkin, J.K. Wenderott, P.F. Green, A.I. Taub, Length dependence of electrostatically induced carbon nanotube alignment, *Carbon N. Y.* 131 (2018) 275–282, <https://doi.org/10.1016/j.carbon.2018.01.014>.
- [39] A. Sen, M. Srivastava, *Regression Analysis: Theory, Methods and Applications*, Springer-Verlag, New York, 1990.
- [40] L. Meng, B. McWilliams, W. Jarosinski, H.-Y. Park, Y.-G. Jung, J. Lee, J. Zhang, Machine Learning in Additive Manufacturing: A Review, *Jom.* 72 (6) (2020) 2363–2377, <https://doi.org/10.1007/s11837-020-04155-y>.
- [41] A.A. Sonin, A generalization of the Pi-theorem and dimensional analysis, *Proc. Natl. Acad. Sci. USA* 101 (2004) 8525–8526, <https://doi.org/10.1073/pnas.0402931101>.
- [42] K. Niendorf, B. Raeymaekers, Quantifying macro- and microscale alignment of carbon microfibers in polymer-matrix composite materials fabricated using ultrasound directed self-assembly and 3D-printing, *Compos. Part A Appl. Sci. Manuf.* 129 (2020), 105713, <https://doi.org/10.1016/j.compositesa.2019.105713>.
- [43] C.E. Ayres, B.S. Jha, H. Meredith, J.R. Bowman, G.L. Bowlin, S.C. Henderson, D. G. Simpson, Measuring fiber alignment in electrospun scaffolds: a user's guide to the 2D fast Fourier transform approach, *J. Biomater. Sci. Polym. Ed.* 19 (2008) 603–621.
- [44] H. Dai, E.W. Wong, C.M. Lieber, Probing Electrical Transport in Nanomaterials: Conductivity of Individual Carbon Nanotubes, *Science (80-)* 272 (1996) 523–526.
- [45] S.J. Ling, J. Sanny, W. Moebs, G. Friedman, S.D. Druger, A. Kolakowska, D. Anderson, D. Bowman, L. Gasparov, L. LaRue, M. Lattery, R. Ludlow, P. Motl, D. Demaree, E.S. Ginsberg, D. Smith, J. Trout, K. Wheelock, T. Pang, K. Podolak, T. Sato, *University Physics, Volume 2*, OpenStax, Houston, Texas, 2016.
- [46] I. Ilyas, X. Chu, *Data Cleaning, first ed.*, Association for Computing Machinery, Waterloo, Ontario, Canada, 2019.
- [47] N.R. Prasad, S. Almanza-Garcia, T.T. Lu, Anomaly detection, *Comput. Mater. Contin.* 14 (2009) 1–22, <https://doi.org/10.1145/1541880.1541882>.
- [48] D.M. Hawkins, The Problem of Overfitting, *J. Chem. Inf. Comput. Sci.* 44 (1) (2004) 1–12, <https://doi.org/10.1021/ci0342472>.
- [49] Scikit-learn Developers, *scikit-learn: Machine Learning in Python*, 2020. <https://scikit-learn.org/stable/>.
- [50] D. Maulud, A.M. Abdulazeez, A Review on Linear Regression Comprehensive in Machine Learning, *J. Appl. Sci. Technol. Trends.* 1, 2020, 140–147. 10.38094/jastt1457.
- [51] M. Goldstein, Bayesian analysis of regression problems, *Biometrika*. 63, 1976, 51–58.
- [52] C. Borgelt, A Naive Bayes Classifier Plug-In for DataEngine, in: *Proc. 3rd Data Anal Symp.*, 1999, pp. 87–90.
- [53] L. Rokach, O. Maimon, *Data Mining with Decision Trees: Theory and Applications*, World Scientific Publishing Co., Hackensack, NJ, USA, 2008.
- [54] L. Breiman, Random Forests, *Mach. Learn.* 45 (2001) 5–32.
- [55] T. Hastie, R. Tibshirani, Discriminant adaptive nearest neighbor classification, *IEEE Trans. Pattern Anal. Mach. Intell.* 18 (1996) 607–616, <https://doi.org/10.1109/34.506411>.
- [56] J. Han, M. Kamber, J. Pei, *Data Mining: Concepts and Techniques*, Third, Elsevier, 2012. https://books.google.com/books?hl=en&lr=&id=pQws07tdpjoC&oi=fnd&pg=PP1&ots=tAFv1YIGW_&sig=wTgGCGYVJr7Su31FauVTbOq1XI#v=onepage&q&f=false.
- [57] C.J. Willmott, S.G. Ackleson, R.E. Davis, J.J. Feddema, K.M. Klink, D.R. Legates, J. O'Donnell, C.M. Rowe, Statistics for the evaluation and comparison of models, *J. Geophys. Res.* 90 (1985) 8995, <https://doi.org/10.1029/jc090ic05p08995>.
- [58] J. Sathesh, S.R. Diwaha, Introduction to radial basis function networks, *Cent. Cogn. Sci. Edinburgh Univ.* (1996). <http://www.anc.ed.ac.uk/~mjo/papers/intro.ps>.
- [59] D.C. Liu, J. Nocedal, On the limited memory BFGS method for large scale optimization, *Math. Program.* 45 (1-3) (1989) 503–528.
- [60] M.-S. Scholz, B.W. Drinkwater, R.S. Trask, Ultrasonic assembly of anisotropic short fibre reinforced composites, *Ultrasonics* 54 (4) (2014) 1015–1019, <https://doi.org/10.1016/j.ultras.2013.12.001>.
- [61] B. Schölkopf, A.J. Smola, *Learning with Kernels: Support Vector Machines, Regularization, Optimization, and Beyond*, The MIT Press, Cambridge, Massachusetts (2002), <https://doi.org/10.7551/mitpress/4175.001.0001>.